Relativistic embedding method: The transfer matrix, complex band structures, transport, and surface calculations

M. James and S. Crampin*
Department of Physics, University of Bath, Claverton Down, Bath BA2 7AY, United Kingdom
(Received 9 November 2009; revised manuscript received 1 March 2010; published 20 April 2010)

We develop the relativistic embedding method for electronic-structure studies. An expression for the transfer matrix is derived in terms of the Green's function of the Dirac equation, and we outline its evaluation within the relativistic embedding framework. The transfer matrix is used to find the complex band structure and an embedding potential that can replace a semi-infinite substrate in *ab initio* electronic-structure calculations. We show that this embedding potential may be used to define an operator that gives the current flowing across a surface; the eigenstates of which define channel functions for conductance studies, and which enable the derivation of a relativistic generalization of the known expression for the conductance across a nanodevice connected to leads. Finally, the application of the embedding potential in relativistic electronic-structure studies is illustrated using an electronlike basis to solve the surface-embedded Dirac equation for Au(111). A calculation with a single layer of atoms within the embedded volume correctly predicts the magnitude of the Rashba-type splitting of the zone center surface state.

DOI: 10.1103/PhysRevB.81.155439 PACS number(s): 71.15.Rf, 73.20.At, 71.70.Ej

I. INTRODUCTION

The embedding method of Inglesfield[1,2] has developed into a powerful tool for performing electronic-structure calculations for extended systems that may be naturally divided into two or more distinct regions. The key advantage of the method is that it enables properties of the entire system to be determined by finding explicit solutions only in a smaller embedded region, with an additional surface operator, the embedding potential, added to the Hamiltonian to ensure the correct matching of wave functions on the surface separating the embedded region from the rest. A particular class of problems where the embedding method is especially useful are semi-infinite systems such as surfaces and interfaces. For example, in contrast to slab and supercell methods, which require large numbers of layers to limit spurious interactions between states localized on opposite surfaces,[3] in embedding calculations surface states, resonances and the bulk continuum are faithfully reproduced and easily distinguishable even in calculations that include just a single surface layer.[4] This can reduce computational demands. Furthermore, because the embedding potential furnishes the surface calculation with details of the bulk band structure, scattering properties needed for photoemission, or tunneling spectroscopy calculations are correctly described, and Fermi surface effects such as surface resistivity can be studied.[5] Exploiting this, recent developments have extended the embedding approach to transport problems and field emission.[6–10] The embedding approach has also been applied to surfaces and interfaces in strongly correlated materials.[11]

Most surface and transport calculations to date using the embedding method have been performed using the scalar-relativistic full potential linearized augmented plane wave method (FLAPW).[4,6,7,12–14] Scalar-relativistic methods and those based on the Schrödinger equation do not include the spin-orbit interaction which is responsible for important effects in many systems, including significant energy shifts and splitting in materials containing heavy elements, determining the spin orientation in crystals (magnetocrystalline anisotropy) and providing mechanisms for spin manipulation in the field of spintronics. Recently an embedding scheme has been developed that is based upon the Dirac equation[15] and which therefore naturally includes the spin-orbit interaction as well as other relativistic effects. In that work the embedding potential used was based upon the reflection matrix obtained from a layer multiple-scattering calculation—an approach that is generally insufficient for complex and open structures.

Here we describe how fully relativistic, full-potential embedding calculations may be performed in the FLAPW framework for both surface and transport problems. The developments are based upon the transfer matrix that describes the relationship between boundary values of the solutions of the Dirac equation across an embedded region and parallel similar advances in the nonrelativistic framework.[6,16] The transfer matrix enables accurate embedding potentials to be obtained for general systems, as well as providing the basis for the calculation of the complex band structure, an important concept in understanding states at surfaces and interfaces. We also derive a generalization of the expression for the conductance across an interface in terms of the embedding potential and the Green's function.

The outline of our work is as follows. First, in Sec. II we summarize the key ideas of the relativistic embedding method and the basis set used in our calculations. In Sec. III we derive an expression for the relativistic transfer matrix and discuss the nonrelativistic limit. We illustrate how the complex band structure may be obtained from the transfer matrix and how the transfer matrix may use to determine an embedding potential to replace a semi-infinite substrate. In Sec. IV we discuss conductance within the embedding framework, identifying surface-orthogonal channel functions and using them to derive an expression for the transmission through an interface in terms of the relativistic embedded Green's function and embedding potentials. Finally in Sec. V we perform a demonstration fully relativistic surface

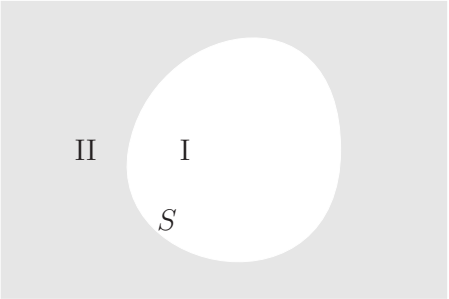

FIG. 1. Geometry for a general embedding problem. The region of interest, region I, is separated from extended region II by surface *S*.

electronic-structure calculation, using an embedding potential derived from the relativistic transfer matrix, reproducing the known dispersion and spin-orbit splitting of the surface state on Au(111) in a one layer calculation.

II. RELATIVISTIC EMBEDDING METHOD

In relativistic embedding problems we are interested in understanding systems described by the single-particle Dirac equation

$$(H-w)\psi=(c\alpha\cdot p+\beta mc^2+V-w)\psi=0, \tag{1}$$

where the Hamiltonian describes an extended system (regions I+II) but the focus of our interest is a small region of space, region I—see Fig. 1. Examples include investigating surface or defect physics or transport properties across an interface. It is also possible to study systems in which a magnetic field is present—for clarity of presentation we only consider the scalar potential in Eq. (1).

Instead of solving Eq. (1) we solve the *embedded* Dirac equation[15]

$$(H+H_S-w)\psi=0 \tag{2}$$

in region I alone, where H_S is a surface operator acting on S, the surface dividing I and II, that ensures solutions of Eq. (2) coincide with solutions of Eq. (1) inside region I

$$H_S\psi(\boldsymbol{r})=ic\hbar\,\boldsymbol{\sigma}\cdot\hat{\boldsymbol{n}}_S(\boldsymbol{r}_S)\,\delta(\boldsymbol{r}-\boldsymbol{r}_S)\times\begin{bmatrix}\psi_s(\boldsymbol{r}_S)-ic\hbar\displaystyle\int_S d^2\boldsymbol{r}'_S\cdot\Gamma(\boldsymbol{r}_S,\boldsymbol{r}'_S;w)\,\boldsymbol{\sigma}\psi_l(\boldsymbol{r}'_S)\\ 0\end{bmatrix}. \tag{3}$$

Here ψ_l and ψ_s refer to the upper and lower two-spinors that make up the Dirac four-spinor ψ, which we refer to as the large (l) and small (s) components on account of their typical relative magnitudes for electron states. The position vector $\boldsymbol{r}_S$ is on S, and $\hat{\boldsymbol{n}}_S(\boldsymbol{r}_S)$ is the surface normal (from I to II) at $\boldsymbol{r}_S$. Γ, which contains all information about region II, is the *relativistic embedding potential*. This 2×2 matrix function relates the amplitudes of small and large components of $\chi(w)$, the solution of the Dirac equation for region II at energy w, on the surface S

$$\chi_s(\boldsymbol{r}_S;w)=ic\hbar\int_S d^2\boldsymbol{r}'_S\cdot\Gamma(\boldsymbol{r}_S,\boldsymbol{r}'_S;w)\,\boldsymbol{\sigma}\chi_l(\boldsymbol{r}'_S;w). \tag{4}$$

Solutions of Eq. (2) satisfy the Dirac equation in I, and also satisfy Eq. (4) on S, thereby correctly matching on to solutions in II. They therefore describe solutions of the Dirac equation for I+II in region I.[15]

Basis

The embedded Dirac Eq. (2) is typically solved by expanding ψ in a suitable basis set and solving the resulting matrix problem. For extended systems it is usually advantageous to actually solve for the corresponding Green's function

$$(H+H_S-w)G(\boldsymbol{r},\boldsymbol{r}';w)=-\delta(\boldsymbol{r}-\boldsymbol{r}'). \tag{5}$$

The choice of basis set is motivated by the need to efficiently describe the spatial variations of the solutions and the boundary values.[8,12,13,17–19] In the present work where we use an all-electron description and our focus is on relativistic systems with underlying two-dimensional translational symmetry, we use a fully relativistic, electronlike linearized augmented plane wave basis set[20] (RLAPW) so that the wave function is expanded in plane waves in the interstitial region and atomiclike solutions in the atomic spheres. In the interstitial region

$$\chi_{\boldsymbol{g}n\sigma}(\boldsymbol{r})=\begin{pmatrix}\phi_\sigma\\ \gamma_k\boldsymbol{\sigma}\cdot\boldsymbol{k}^+\phi_\sigma\end{pmatrix}e^{i\boldsymbol{k}^+\cdot\boldsymbol{r}}\pm\begin{pmatrix}\phi_\sigma\\ \gamma_k\boldsymbol{\sigma}\cdot\boldsymbol{k}^-\phi_\sigma\end{pmatrix}e^{i\boldsymbol{k}^-\cdot\boldsymbol{r}}, \tag{6}$$

where the $\pm$ sign determines whether the z dependence of the large component is sin-like or cos-like, as in corresponding nonrelativistic implementations of the embedding method.[12,13,19] The wave vectors in Eq. (6) are $\boldsymbol{k}^\pm=\boldsymbol{k}_\parallel+\boldsymbol{g}\pm k_n\hat{\boldsymbol{z}}$ where $\boldsymbol{k}_\parallel$ is a wave vector in the two-dimensional Brillouin zone, $\boldsymbol{g}$ is a two-dimensional reciprocal lattice vector, and the components in the $\hat{\boldsymbol{z}}$ direction are defined over the interval $[0:L]$, $k_n=2n\pi/L$. L is greater than the length of the embedded region so that the basis functions have a range of amplitudes on S (see Sec. V). The ϕ_σ are the usual Pauli two-spinors and $\gamma_k=c\hbar/(W_k+mc^2)$ with $W_k=\sqrt{c^2\hbar^2k^2+m^2c^4}$. These basis functions are extended into the atomic sphere as linear combinations of the radial solutions of the Dirac equation and their energy derivatives for the spherical component of the atomic potential at that site, found at some pivot energy W^α_κ. In sphere α at $\boldsymbol{R}_\alpha$

$$\chi_{\boldsymbol{g}n\sigma}(\boldsymbol{r})=\sum_\Lambda\left[A^{\alpha\Lambda}_{\boldsymbol{g}n\sigma}u^\alpha_\Lambda(\boldsymbol{r}_\alpha)+B^{\alpha\Lambda}_{\boldsymbol{g}n\sigma}\dot{u}^\alpha_\Lambda(\boldsymbol{r}_\alpha)\right], \tag{7}$$

where $\Lambda=(\kappa,\mu)$, $\boldsymbol{r}_\alpha=\boldsymbol{r}-\boldsymbol{R}_\alpha$, $\dot{u}=\partial u/\partial W$, and

$$u^\alpha_\Lambda(\boldsymbol{r})=\begin{bmatrix}g^\alpha_\kappa(r)\Omega_{\kappa,\mu}(\hat{\boldsymbol{r}})\\ if^\alpha_\kappa(r)\Omega_{-\kappa,\mu}(\hat{\boldsymbol{r}})\end{bmatrix} \tag{8}$$

with $\Omega_{\kappa,\mu}(\hat{\boldsymbol{r}})$ the usual linear combination of spherical harmonics. The coefficients $A^{\alpha\Lambda}_{\boldsymbol{g}n\sigma}$ and $B^{\alpha\Lambda}_{\boldsymbol{g}n\sigma}$ may be chosen by matching amplitudes of large and small components at the surface of the spheres, or alternatively by matching both amplitude and derivative of the large component. This "elec-

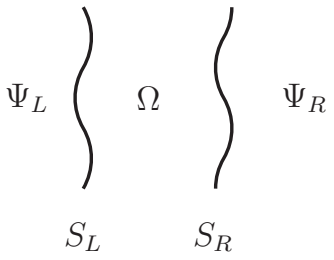

FIG. 2. Geometry for a general definition of the transfer matrix, T_Ω, which relates the amplitude of a wave function on surface S_L, ψ_L, to that on surface S_R, ψ_R.

tronlike" basis prevents variational collapse[21] to negative energy solutions of the Dirac equation while enabling an accurate solution of Eq. (2) or Eq. (5) for layered systems. The additional spin index in the basis functions means basis sets used in this relativistic formulation are twice the size of those used in conventional embedding studies.

III. TRANSFER MATRIX

The transfer matrix is a powerful tool in nonrelativistic calculations, playing a key role in studies of complex band structures,[16] transport properties,[6] and, of particular significance here, in deriving embedding potentials for use in electronic-structure calculations involving semi-infinite substrates.[13] In this section we show how the idea of the transfer matrix can be implemented in a fully relativistic framework.

To define the transfer matrix we consider a system in which a region of space Ω extends infinitely in two dimensions and is finite in one dimension, bounded by surfaces S_L and S_R—see Fig. 2. The transfer matrix T_Ω relates the amplitude of the wave function on S_L, Ψ_L, to the amplitude on S_R, Ψ_R

$$\Psi_R = T_\Omega \Psi_L. \tag{9}$$

Starting from the Dirac equation, it can be shown[15] that the wave function at position $\boldsymbol{r}$ in Ω may be related to its amplitude on the bounding surface through the Green's function G

$$\Psi(\boldsymbol{r}) = -ic\hbar \int_S d^2\boldsymbol{r}_S \cdot G(\boldsymbol{r},\boldsymbol{r}_S)\boldsymbol{\alpha}\Psi(\boldsymbol{r}_S). \tag{10}$$

Here $S=S_L \cup S_R$ and the surface normal is out of Ω. This result is independent of the boundary conditions satisfied by G so choosing G_{ls} to vanish on S_L and S_R gives

$$\psi_{Ll} = F_{LR}\psi_{Rs} + F_{LL}\psi_{Ls},$$

$$\psi_{Rl} = F_{RR}\psi_{Rs} + F_{RL}\psi_{Ls}, \tag{11}$$

where position vectors are suppressed and multiplication implies integration over the appropriate surface. ψ_{Ll} is the large component of the wave function on S_L, $F_{LR}=-ic\hbar G_{ll}(\boldsymbol{r}_L,\boldsymbol{r}'_R)\boldsymbol{\sigma}\cdot\hat{\boldsymbol{n}}_R(\boldsymbol{r}'_R)$ etc. Note that in obtaining these relations we allow $\boldsymbol{r}$ in II to approach the surface from within Ω, establishing the distinct ordering when Green function arguments $\boldsymbol{r}_S$ and $\boldsymbol{r}'_S$ are on the same surface. Rearranging Eq. (11), we may therefore construct the transfer matrix as

$$T_\Omega = \begin{pmatrix} F_{RR}F_{LR}^{-1} & F_{RL} - F_{RR}F_{LR}^{-1}F_{LL} \\ F_{LR}^{-1} & -F_{LR}^{-1}F_{LL} \end{pmatrix}. \tag{12}$$

The transfer matrix only involves the large-large component of the Green's function for region Ω. In the following section we illustrate this for a problem that can be solved analytically. More generally we calculate T_Ω with the embedding formalism. In this case in Eq. (5) we put $H_S=H_L+H_R$, and then set to zero the left and right embedding potentials. This variationally imposes the boundary condition that the small component of the Green's function vanishes on S_L and S_R that was assumed in deriving the transfer-matrix expression.

At this point it is interesting to consider the nonrelativistic limit of the transfer matrix in Eq. (12) by letting $c\to\infty$. In this limit the large component of the wave function reduces to a nonrelativistic wave function (with appropriate Pauli two-spinor) and the small component, being of order $1/c$, vanishes. In general, G_{ll} becomes the nonrelativistic Green's function and all other components vanish. It is clear that F_{LR} etc. are of order c and a nonrelativistic limit of these quantities is ill defined. Regarding the transfer matrix, T_{ll} and T_{ss} persist as $c\to\infty$, T_{sl} is of order $1/c$ and vanishes, while T_{ls}, which is order c, is ill defined. To regularize the limit we introduce the transformation $\tilde{\Psi}_S=C_S\Psi_S$, $\tilde{T}_\Omega=C_R T_\Omega C_L^{-1}$ with

$$C_S(\boldsymbol{r}_S,\boldsymbol{r}'_S) = \begin{pmatrix} 1 & 0 \\ 0 & i\dfrac{w - v(\boldsymbol{r}_S) + mc^2}{c\hbar}\sigma_S(\boldsymbol{r}_S) \end{pmatrix}\delta(\boldsymbol{r}_S - \boldsymbol{r}'_S). \tag{13}$$

The transfer matrix becomes as $c\to\infty$

$$\tilde{T}_\Omega \to \begin{pmatrix} G_{RR}G_{LR}^{-1} & -\dfrac{\hbar^2}{2m}[G_{RL} - G_{RR}G_{LR}^{-1}G_{LL}] \\ -\dfrac{2m}{\hbar^2}G_{LR}^{-1} & -G_{LR}^{-1}G_{LL} \end{pmatrix}, \tag{14}$$

which is formally identical to the expression for the nonrelativistic transfer matrix in terms of the Green's function[16] although here the entries are 2×2 quantities.

The reason we must make the transformation in Eq. (13) in order to recover the nonrelativistic limit is as follows. The Schrödinger equation is second order in space, meaning that both the amplitude and first derivative of the wave function must be specified on S_L and S_R to properly define a transfer matrix. In contrast, the Dirac equation is first order in space and only the amplitude of the wave function must be specified in the bounding surfaces. However, the small component may be expressed in terms of the first derivative of the large component but a prefactor which varies like $1/c$ as $c\to\infty$ means it vanishes and only the large component survives in the limit. The transformation in Eq. (13) ensures that it persists.

Despite the identical appearance of the $c\to\infty$ limit of $\tilde{T}$ and the nonrelativistic transfer matrix,[16] there are significant differences. In practice the 2×2 blocks in Eq. (14) are not diagonal when the Green's function is required to satisfy the

boundary conditions leading to Eq. (11), and indeed the transformation in Eq. (13) gives

$$\tilde{\Psi} = \begin{pmatrix} \psi_l \\ \partial_{n_S}\psi_l + i\boldsymbol{\sigma}\cdot[\hat{\boldsymbol{n}}_S \times \boldsymbol{\nabla}\psi_l] \end{pmatrix} \tag{15}$$

the second term in the lower component being an additional term not present in the nonrelativistic theory.

A. Analytic example

An illustrative example which may be treated analytically is a region Ω of constant potential v, between parallel planes S_L and S_R at $z=L$ and $z=R$ respectively, with $R-L=d$. The resulting transfer matrix can be used, e.g., to study scattering by piecewise constant potentials.

Translational invariance parallel to the planes reduces the problem to finding the wave-vector-resolved transfer matrix $T_{\Omega,\boldsymbol{k}_\parallel}$. At energy w and wave-vector $\boldsymbol{k}_\parallel$ solutions of the Dirac equation in Ω with zero-amplitude small component at $z=0$ are

$$\psi_{\boldsymbol{k}_\parallel,\sigma}(z) = \begin{pmatrix} \dfrac{c(\hbar\boldsymbol{\sigma}_\parallel\cdot\boldsymbol{k}_\parallel + \sigma_z p_z)}{w-v-mc^2}\sin k_z z\,\phi_\sigma \\ \sin k_z z\,\phi_\sigma \end{pmatrix}, \tag{16}$$

where $k_z = \sqrt{(w-v)^2 - m^2c^4 - c^2\hbar^2k_\parallel^2}/c\hbar$. From these, the Green's function which satisfies the zero-amplitude small component boundary conditions on $z=L$ and $z=R$ may be constructed by the direct method; for $z<z'$

$$G_{\boldsymbol{k}_\parallel,\sigma}(z,z') = \frac{w-v-mc^2}{c^2\hbar^2 k_z \sin k_z(R-L)} \times \psi_{\mathbf{k}_\parallel,\sigma}(z-L)\psi^{\times}_{\mathbf{k}_\parallel,\sigma}(z'-R) \tag{17}$$

with L and R in the wave function interchanged when $z>z'$. Placing z' and then z on the surface planes from within Ω one finds, e.g.,

$$F_{LL} = \frac{ic\hbar}{w-v-mc^2}\begin{bmatrix} k_z\cot k_z d & -i(k_x-ik_y) \\ -i(k_x+ik_y) & -k_z\cot k_z d \end{bmatrix} \tag{18}$$

and eventually the transfer matrix

$$T_{\Omega,\boldsymbol{k}_\parallel} = \begin{pmatrix} \cos k_z d & -\dfrac{i(k_x-ik_y)}{k_z}\sin k_z d & \dfrac{i(w-v+mc^2)}{c\hbar k_z}\sin k_z d & 0 \\ \dfrac{i(k_x+ik_y)}{k_z}\sin k_z d & \cos k_z d & 0 & -\dfrac{i(w-v+mc^2)}{c\hbar k_z}\sin k_z d \\ \dfrac{i(w-v-mc^2)}{c\hbar k_z}\sin k_z d & 0 & \cos k_z d & -\dfrac{i(k_x-ik_y)}{k_z}\sin k_z d \\ 0 & -\dfrac{i(w-v-mc^2)}{c\hbar k_z}\sin k_z d & \dfrac{i(k_x+ik_y)}{k_z}\sin k_z d & \cos k_z d \end{pmatrix}. \tag{19}$$

The ll block, which is unaltered by the transformation $T\to\tilde{T}$ introduced in the previous section and which therefore survives unchanged in the $c\to\infty$ limit, is not diagonal, demonstrating the difference with the nonrelativistic transfer matrix obtained in Ref. 16. Only for $\boldsymbol{k}_\parallel=0$, when the momentum is parallel to the spin-quantization axis, do we recover an identical form

$$\tilde{T}_{\Omega,\boldsymbol{k}_\parallel=0} = \begin{pmatrix} \cos k_z d\mathbb{1} & -k_z^{-1}\sin k_z d\mathbb{1} \\ -k_z\sin k_z d\mathbb{1} & -\cos k_z d\mathbb{1} \end{pmatrix}. \tag{20}$$

B. Complex band structure

Assume that region Ω in the transfer matrix problem is a representative layer (containing one or more planes of atoms) of a bulk crystal which has three-dimensional translational symmetry. Such a layer can reproduce the bulk crystal by repetition in directions normal ($\hat{\boldsymbol{z}}$) to the layers with an associated layer-layer translation vector $\boldsymbol{d}$ that reflects the translational periodicity of the solid and also takes surface S_L to S_R—see Fig. 3. It follows that Bloch states of the crystal satisfy

$$\Psi_R = e^{i\boldsymbol{k}\cdot\boldsymbol{d}}\Psi_L \tag{21}$$

and comparing with Eq. (9) we see that solutions of the eigenvalue problem[16]

$$\int_{S_L} d^2r'_L T_\Omega(\boldsymbol{r}_L+\boldsymbol{d},\boldsymbol{r}'_L)\psi(\boldsymbol{r}'_L) = \lambda\psi(\boldsymbol{r}_L) \tag{22}$$

yields eigenvectors that are Bloch states on S_L corresponding to eigenvalues $\lambda = e^{i\boldsymbol{k}\cdot\boldsymbol{d}}$.

At real energies, eigenstates of T_Ω with eigenvalues that satisfy $|\lambda|=1$ have real wave vectors $\boldsymbol{k}$ that are part of the conventional band structure of the solid. Those with $k_z>0$ are right propagating Bloch states and those with $k_z<0$ are left propagating Bloch states. Alongside these solutions are others for which $|\lambda|\neq 1$, corresponding to solutions with complex wave vectors with imaginary values of k_z. These form the *complex band structure*. The associated wave functions have an exponentially varying envelope, decaying to

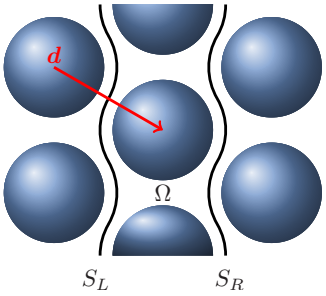

FIG. 3. (Color online) Geometry for calculating the transfer matrix in the bulk. Adjacent layers are related by a translation $\boldsymbol{d}$. The transfer matrix connects states on surface S_L across region Ω to states on surface S_R.

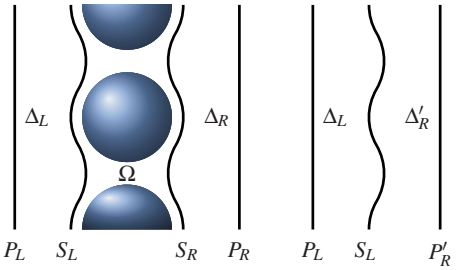

FIG. 4. (Color online) Geometry of embedding regions used in practical embedding calculations. Left: buffer regions Δ_L, Δ_R extend Ω so that the combined region has planar bounding surfaces, P_L, P_R. Right: the auxiliary problem involving regions Δ_L and Δ'_R, bounded by surfaces P_L and P'_R.

the left (right) if $|\lambda|>1$ (<1). Such evanescent waves do not satisfy physical boundary conditions for an infinite bulk crystal but may persist if this translational symmetry is broken, for example, by a surface or interface. In these situations screening confines modification of the potential to a few layers close to the surface/interface, beyond which the potential is bulklike and where the wave function may include contributions that decay into the crystal. Indeed in band gaps there are no states with real $\boldsymbol{k}$ and it is the magnitudes of the imaginary allowed k_z that determine the decay of localized states away from interfaces,[22] and tunneling across metal/insulator/metal junctions.[23] In general the evanescent Bloch states are essential for a complete description of scattering. The transfer matrix given in Eq. (12) enables the complex band structure to be determined accurately in general systems when relativistic effects are significant.

As an example, for the analytic case studied in Sec. III A it is straightforward to show that the four eigenvalues of $T_{\Omega,\boldsymbol{k}_\parallel}$ are the twofold degenerate pair $\lambda_\pm = e^{\pm ik_z d}$ and that the corresponding (unnormalized) eigenvectors may be chosen to be

$$U^{\pm}_{\boldsymbol{k}_\parallel,\sigma} = \begin{pmatrix} \phi_\sigma \\ \dfrac{c\hbar\boldsymbol{\sigma}\cdot(\boldsymbol{k}_\parallel \pm k_z\hat{\boldsymbol{z}})}{w - v + mc^2}\phi_\sigma \end{pmatrix}, \tag{23}$$

which as expected describe the amplitudes on S_L of Bloch states with wave vector $\boldsymbol{k}_\parallel \pm k_z\hat{\boldsymbol{z}}$.

For realistic systems the complex band structure can be obtained by diagonalizing the numerically determined transfer matrix. To do so it is first necessary to identify the region Ω, or equivalently the surfaces S_L and S_R. The nature of electron wave functions (and Green's functions) in solids is such that it is not normally possible to identify suitable surfaces for this purpose that enable a numerical representation that is both efficient and straightforward. A surface on which the wave function is relatively smooth must weave between atomic cores, complicating the identification of suitable surface expansion functions while a planar surface that affords a routine surface expansion will normally cut through cores and require a large number of expansion functions to accurately describe the rapid spatial variations.

Solutions to this problem involve transforming the problem on curvy surfaces S_L, S_R to an equivalent problem stated on planar surfaces.[12,13,19,24] Here we adapt the approach of Ref. 16 to the relativistic case. Buffer regions Δ_L and Δ_R are introduced to either side of Ω as in Fig. 4 so that the new volume $\Omega' = \Delta_L \cup \Omega \cup \Delta_R$ has planar surfaces P_L and P_R. A subsidiary problem is introduced containing the space $\Omega'' = \Delta_L \cup \Delta'_R$, where Δ'_R is region Δ_R translated by $-\boldsymbol{d}$. The potential in the buffer regions is arbitrary but for practical purposes is chosen to be smoothly varying, for example, a constant or the smooth extension of the interstitial expansion into these regions. The transfer matrices $T_{\Omega'}$ and $T_{\Omega''}$ are found using Eq. (12) where the surface integrals that are now required are taken over planar surfaces well removed from atomic cores, which are straightforward to perform. In terms of the transfer matrices for the individual regions we have

$$T_{\Omega'} = T_{\Delta_R} T_\Omega T_{\Delta_L}, \quad T_{\Omega''} = T_{\Delta'_R} T_{\Delta_L} \tag{24}$$

and one can show that

$$T = T_{\Omega'} T^{-1}_{\Omega''} \equiv T_{\Delta_R} T_\Omega T^{-1}_{\Delta'_R} \tag{25}$$

satisfies an eigenvalue equation similar to Eq. (22) but with position vectors on P'_R not S_L, and with the same eigenvalues as T_Ω. Hence the complex band structure may be obtained by constructing and diagonalizing T, which only involves expansions on, and integrals over, planar surfaces.

Using the RLAPW basis, contraction of the Green's function expansions onto the planar surfaces leads to surface expansion in basis functions

$$\chi_\nu(\boldsymbol{r}_\parallel) = \frac{1}{\sqrt{A}} e^{i(\boldsymbol{g}+\boldsymbol{k}_\parallel)\cdot\boldsymbol{r}_\parallel}\phi_\sigma \tag{26}$$

at wave vector $\boldsymbol{k}_\parallel$, where $\nu = (\boldsymbol{g}, \sigma)$ is a composite index and the complex band structure is obtained from the explicit eigenvalue problem

$$\sum_{\nu'} e^{i\boldsymbol{g}\cdot\boldsymbol{d}_\parallel} T_{\nu\nu'} \Upsilon_{\nu'} = e^{ik_z d_z} \Upsilon_\nu. \tag{27}$$

Figure 5 shows results obtained for Au(111). In this calculation the planes P_L and P_R (Fig. 4) have been placed 2.7 a.u. to either side of the plane of atoms and the potential within the buffer region is the continuous extension of the plane wave expansion of the interstitial potential into these regions. We use a basis set containing 19 $\boldsymbol{g}$ vectors. The real bands

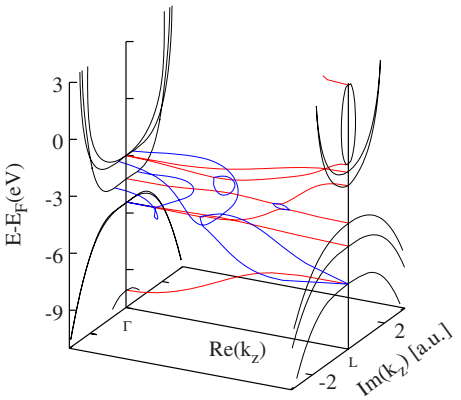

FIG. 5. (Color online) Complex band structure for Au(111) found from the transfer matrix evaluated at $\boldsymbol{k}_{\parallel}=0$. Only the bands with $|\mathrm{Im}(k_z)| \leq \pi$ are shown.

are in excellent agreement with previous results and the complex bands show their continuation into the complex plane.[25] We see loops connect extrema of the real bands with Λ_6 symmetry. One connects the L_{6^-} level near −7.6 eV with a band minimum with $k_z \approx 0.3\Gamma L$ and smaller loops connecting extrema away from the high symmetry points are found centered on $k_z \approx 0.5\Gamma L$ and $0.7\Gamma L$. The L_{6^-} and L_{6^+} levels below and above E_F are also connected by a complex band with $\mathrm{Re}(k_z)=L$. In the (E,k_z) range show in Fig. 5 two loops connect extrema of the real bands with extrema away from the real k axis. The Λ_{4+5} band extrema at $E=-5.3$ eV is connected to a minimum of the complex bands with $E=-3.0$ eV and $\mathrm{Re}(k_z)=\Gamma$, and the Λ_6 band extreme at $E=-5.4$ eV connects with the complex band with $E=-4.2$ eV and $\mathrm{Re}(k_z)=\Gamma$. Finally, we mention that Dal Corso *et al.*[26] have recently reported a scheme for calculating relativistic complex bands that employs two-component wave functions and relativistic pseudopotentials—here the bands are found from an all-electron four-component solution of the full Dirac equation.

C. Embedding potential

Another application of the transfer matrix is to generate the embedding potential for a semi-infinite bulk crystal, for subsequent surface or interface studies. In Eq. (4) the embedding potential at energy w relates the amplitudes on S of small and large components of χ, a solution of the Dirac equation at energy w in II. If II corresponds to a semi-infinite left substrate then χ can be expressed as a linear combination of outgoing Bloch states, i.e., either decaying to the left or with $k_z<0$. The surface values on S_L of these Bloch states are given by the eigenvectors of the transfer matrix and it follows that the embedding potential may be found by inverting a matrix of eigenvectors of the transfer matrix. An embedding potential for a semi-infinite right substrate is similarly obtained from the Bloch states that decay or carry flux to the right.[16]

It is once again beneficial to work on planar surfaces. An eigenstate Υ_j of T in Eq. (25) is defined on surface P'_R (Fig. 4) and is related to the eigenstate ψ_j of T_Ω with the same

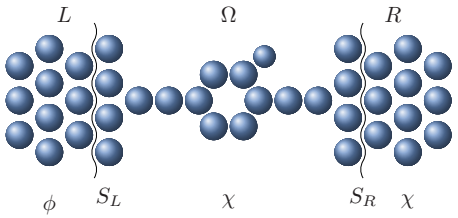

FIG. 6. (Color online) Geometry for studying conductance across a nanodevice in region Ω, connecting left (L) and right (R) leads. S_L and S_R are dividing surfaces. In the left lead ϕ describes a state carrying current toward S_L; this extends into $\Omega+R$ as χ, in R carrying current away from S_R to the right.

eigenvalue by $\psi_j=T^{-1}_{\Delta'_R}\Upsilon_j$; hence $\Psi_j=T^{-1}_{\Omega''}\Upsilon_j$ is the amplitude on plane P_L of the Bloch state ψ_j back propagated from S_L, and can be used to derive an embedding potential for a left substrate on the proviso that the buffer region is also included in the subsequent embedded system calculation. Using surface expansion functions in Eq. (26) we obtain

$$\Gamma_{\nu\nu'} = \frac{i}{c\hbar}\sum_j [\Psi_s]_{\nu j}[\Psi_l^{-1}]_{j\nu'}\sigma_{z,\sigma'\sigma'}, \tag{28}$$

where $[\Psi_s]$ is a matrix formed of the small components of transferred eigenvectors Ψ_j corresponding to outgoing Bloch states of the left substrate and $[\Psi_l^{-1}]$ is the inverse of the corresponding matrix of large components.

IV. CHANNEL FUNCTIONS AND TRANSPORT

The ability to handle extended substrates makes the embedding scheme attractive for ballistic transport studies of "nanodevices." Embedding potentials may be used to replace current carrying leads so that only the device region, region Ω in Fig. 6, needs to be explicitly treated. Conduction through the device region Ω results from electrons being transmitted from open channels in the left-hand lead, through Ω and into the open channels in the right hand lead. Calculations of the conduction therefore reduce to calculation of the transmission probability between open channels in the leads. Here we show how this can be found in the relativistic formulation.

In relativistic theory the probability current J_S carried across surface S by state ψ is

$$J_S = c\int_S d^2\boldsymbol{r}_S \cdot \psi^\dagger(\boldsymbol{r}_S)\boldsymbol{\alpha}\psi(\boldsymbol{r}_S). \tag{29}$$

Expanding ψ into its large and small components, and using Eq. (4) to replace ψ_s, we obtain for the current

$$J_S = c^2\hbar\int_S d^2r_S\int_S d^2r'_S\psi_l^\dagger(\boldsymbol{r}_S)\Sigma(\boldsymbol{r}_S,\boldsymbol{r}'_S)\psi_l(\boldsymbol{r}'_S), \tag{30}$$

where

$$\Sigma(\boldsymbol{r}_S,\boldsymbol{r}'_S) = i\sigma_S(\boldsymbol{r}_S)[\Gamma(\boldsymbol{r}_S,\boldsymbol{r}'_S) - \Gamma^\dagger(\boldsymbol{r}'_S,\boldsymbol{r}_S)]\sigma_S(\boldsymbol{r}'_S). \tag{31}$$

Thus the current may be obtained from the large component of the wave function and the embedding potential evaluated

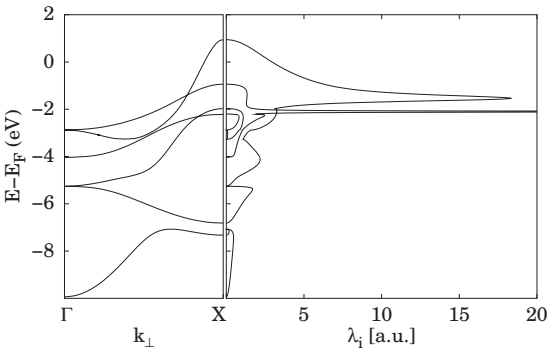

FIG. 7. Au(001) interface at $\boldsymbol{k}\|=0$. Left: band structure in the ΓX direction; right: eigenvalues of $\Sigma_{\boldsymbol{k}_\|=0}$ evaluated on an embedding plane midway between atomic planes.

at the energy of the state ψ. Our convention for the surface normals when embedding region Ω means that, when applied to the geometry of Fig. 6, J_S is the current flowing in the direction *into* the left (right) lead when S is L (R).

A. Channel functions

The eigenfunctions of Σ, which satisfy

$$\int_S d^2r_S \Sigma(\boldsymbol{r}_S,\boldsymbol{r}'_S)u_i(\boldsymbol{r}'_S) = \lambda_i u_i(\boldsymbol{r}_S) \tag{32}$$

can be used to define channel functions of the lead associated with S. Since Σ is Hermitian, its eigenvalues $\{\lambda_i\}$ are real and its eigenfunctions $\{u_i\}$ may be chosen to be orthogonal over S. The 2×2 nature of Σ means that the functions u_i are 2×1 spinors; we can identify these as the surface values of the large components of an extended function ψ_i, whose small component on S may be found from the embedding potential, Eq. (4), and whose value within the lead may be found from the Green function for the lead using Eq. (10). Thus u_i fully determines a channel function ψ_i. With u_i normalized over S it follows from Eqs. (30) and (32) that the current across S associated with channel function ψ_i is $J_i = c^2\hbar\lambda_i$, and hence $\lambda_i \geq 0$ as a result of the outgoing boundary conditions implicit in the embedding potential. Nonzero λ_i correspond to current-carrying or open channels and zero eigenvalues correspond to closed channels (evanescent ψ_i). Expanding Σ in terms of its eigenfunctions, we then have

$$\Sigma(\boldsymbol{r}_S,\boldsymbol{r}'_S) = \sum_i \lambda_i u_i(\boldsymbol{r}_S)u_i^\dagger(\boldsymbol{r}'_S), \tag{33}$$

where the sum need only be taken over open channels.

Figure 7 shows the eigenvalues of Σ at $\boldsymbol{k}_\|=(0,0)$ for a semi-infinite Au(001) substrate, alongside the conventional band structure. In this calculation the embedding plane is positioned midway between atomic planes.

Bloch states, which are commonly used as channel functions in conductance studies are orthogonal functions within the volume of the lead but not in general orthogonal on S; in contrast, the embedding channel functions are orthogonal on S but not in general in the volume of the leads. The surface orthogonality of the embedding channel functions is attractive as this is precisely where the channel functions are required in calculating the conductance and their orthogonality provides new opportunity for interpreting how the nanodevice in Ω conducts between left and right leads.

B. Conductance

We now consider the conductance through a nanostructure with device region Ω sandwiched between leads, as in Fig. 6. An *incoming* state from the left lead L, ϕ, is transmitted across Ω into outgoing states in the right lead R. These leads will be replaced by embedding potentials acting on S_L and S_R, respectively, and the problem will be solved in Ω alone.

The embedding potential introduced in Sec. II relates small and large components of *outgoing* states, being evaluated at energy $w+i\delta$, where δ is a positive infinitesimal. In the conductance problem we have an *incoming* state ϕ in the left lead, which is a time-reversed outgoing state. In relativistic theory the time reversal operator is $\hat{K}=-i\sigma_y^{(4)}\hat{K}_0$ where $\hat{K}_0$ is the complex conjugation operator[27] so that $\phi=\hat{K}\psi$ where ψ is an outgoing state. Using Eq. (10) this enables us to express the large component of the wave function in $\Omega+R$ in terms of the large-large component of the Green's function and Σ for the left lead

$$\chi_l(\boldsymbol{r}) = ic^2\hbar^2 \int_{S_L} d^2r_L \int_{S_L} d^2r'_L G_{ll}(\boldsymbol{r},\boldsymbol{r}_L) \times \hat{K}\Sigma_L(\boldsymbol{r}_L,\boldsymbol{r}'_L)\hat{K}^\dagger \phi_l(\boldsymbol{r}'_L). \tag{34}$$

We now assume that the incoming state corresponds to an open channel function of the left lead, $Ku_{L,i}$, and expand the transmitted state on S_R as a sum over channel functions of the right lead, $\chi_l(\boldsymbol{r}_R)=\Sigma_j t_{ij}u_{R,j}(\boldsymbol{r}_R)$, where t_{ij} is a transmission coefficient. If now the channel functions are normalized to carry unit current $(c^2\hbar\lambda_i\int_S d^2r_S|u_{S,i}(\boldsymbol{r}_S)|^2=1)$ then

$$t_{ij} = ic^4\hbar^3\lambda_i\lambda_j \int_{S_L} d^2r_L \int_{S_R} d^2r_R u_j^\dagger(\boldsymbol{r}_R) \times G_{ll}(\boldsymbol{r}_R,\boldsymbol{r}_L)v_i(\boldsymbol{r}_L). \tag{35}$$

The current through the device region is proportional to the transmission probability $T_{ij}=|t_{ij}|^2$ summed over all open channels, where each channel function carries the same flux as may be shown by demonstrating a unitary transformation relates them to the corresponding set of Bloch states.[9] Making use of the property of the time-reversed Green's function, $\hat{K}G(\boldsymbol{r},\boldsymbol{r}')\hat{K}^\dagger = G^\dagger(\boldsymbol{r}',\boldsymbol{r})$, along with Eq. (32), we find that the transmission is given by

$$\sum_{ij} T_{ij} = (c^2\hbar^2)^2 \mathrm{Tr}\, \hat{K}\Sigma_L G_{LR}\hat{K}^\dagger\Sigma_R G_{RL}, \tag{36}$$

where position arguments have been suppressed for brevity and where the trace is taken over both spin and position variables. Transmission through the device region, Ω, may therefore be determined fully relativistically, using the large-large part of the Green's function calculated only in Ω (which may be found via embedding), and the embedding potentials for the leads. This result generalizes corresponding

nonrelativistic expressions.[6,9] The appearance of the time-reversal operation in Eq. (36) may be explained by recognizing the Green's function as a propagator. Beginning at the right-hand side, $\Sigma(\boldsymbol{r}'_R,\boldsymbol{r}_R)G_{ll}(\boldsymbol{r}_R,\boldsymbol{r}_L)$ describes propagation from S_L to S_R, the direction of the current and $\Sigma(\boldsymbol{r}_L,\boldsymbol{r}'_L)G_{ll}(\boldsymbol{r}'_L,\boldsymbol{r}'_R)$ describes propagation from S_R to S_L but is time reversed and so is also in the direction of the current.

V. EMBEDDED SURFACE CALCULATIONS

A class of problems to which the embedding method is particularly well suited is calculation of the electronic structure of surfaces and we demonstrate here a relativistic surface embedding calculation with Au(111). We choose this system because it has a well-characterized surface state[28] which through a combination of the broken inversion symmetry at the surface and the relativistic spin-orbit interaction exhibits a spin-split Rashba-type dispersion

$$E(\boldsymbol{k}) \simeq E_0 + \frac{\hbar^2(k \pm k_0)^2}{2m^*}. \tag{37}$$

Furthermore, this state has particular properties that provide a stringent test of the extent to which the embedding potential correctly reproduces the influence of an extended substrate when added to the Hamiltonian of the surface region of a crystal. First, it is known from previous studies (e.g., Ref. 29) that the Au(111) surface state extends a significant distance into the crystal, making it especially sensitive to the crystal potential beneath the surface layers. An illustration of this comes from the magnitude of the interaction seen in thin film or periodic supercell calculations for Au(111), where surface states that form on one crystal face are sensitive to the presence of the second, resulting in an energy splitting.[3] find the magnitude of this is in excess of 500 meV for seven-layer slabs and only becomes less that 10 meV for slab thicknesses greater than 23 layers. Second,[30] have exploited the fact that the dominant contribution to the spin-orbit interaction originates from the potential in a small volume surrounding each nucleus to decompose the spin-orbit splitting into layer by layer contributions. They find only $\simeq$58% of the splitting may be attributed to the spin-orbit interaction in the surface layer with successively deeper layers accounting for 25%, 11% and 4%. Thus the subsurface region makes an important contribution to the total relativistic effect on the Au(111) surface state.

In our calculations we use an embedded region containing the outermost or the three outermost atomic layers of the surface. The semi-infinite substrate is incorporated via an embedding potential that is found from the transfer matrix as outlined in Sec. III C. This embedding potential provides a formally exact replacement of the influence of the semi-infinite substrate on the electron wave functions in the embedded region.[15] In the surface calculation, by calculating the embedding potential from the transfer matrix there is made the implicit assumption that the Hamiltonian for the substrate is "bulklike" up to the embedding surface, i.e., the effective potential is unchanged from that deep in the bulk. In metallic systems screening is efficient so that for close-packed surfaces this condition holds to a sufficient degree even after just one or two layers, whereas more would be required for open surfaces or nonmetallic systems. The geometry is shown in Fig. 8. The buffer region, Δ_L, introduced when transferring the bulk embedding potential Γ_L from the curvy surface S_L to the plane P_L, is also included as is required in order to properly compensate and ensure that the Green's function in the surface region correctly matches to that in the bulk. On the vacuum side the space beyond which the potential is assumed to be uniform (in our calculations chosen to be $\sim$8 Å beyond the outermost atomic plane) is incorporated via another embedding potential, for which we use an analytic expression. This is derived from Eq. (4) using for χ a general outgoing wave function for this constant potential. This gives

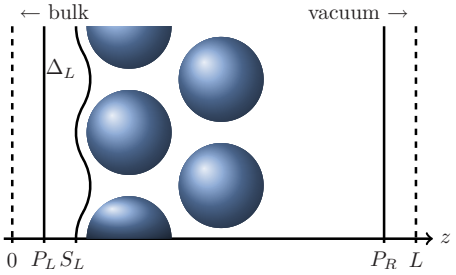

FIG. 8. (Color online) The geometry for an embedded surface calculation. Embedding potentials act on planes P_L (substrate embedding potential) and P_R (vacuum embedding potential); buffer region Δ_L extends from P_L to S_L, beyond which the actual surface potential applies.

$$\Gamma_R(\boldsymbol{r}_S,\boldsymbol{r}'_S;w) = \int \frac{d^2k_\parallel}{(2\pi)^2}\Gamma_{\boldsymbol{k}_\parallel}(w)e^{i\boldsymbol{k}_\parallel\cdot(\boldsymbol{r}_S-\boldsymbol{r}'_S)} \tag{38}$$

with

$$\Gamma_{\boldsymbol{k}_\parallel}(w) = \frac{-i}{w - v_{\text{vac}} + mc^2}\begin{bmatrix} k_z(k_\parallel,w) & -k_x + ik_y \\ +k_x + ik_y & k_z(k_\parallel,w) \end{bmatrix}, \tag{39}$$

where $k_z(k_\parallel,w)=\sqrt{(w-v_{\text{vac}})^2-m^2c^4-\hbar^2k_\parallel^2c^2}/\hbar c$ and v_{vac} is the vacuum level measured relative to the zero of energy. Our attention is focused on the surface state near E_F, for which the constant vacuum potential beyond P_R is a suitable approximation. It is also possible to derive an analytic embedding potential for an imagelike potential, which would be necessary for studying relativistic effects on states nearer the vacuum level.[31]

The embedded Green's function at energy w, $G(w)$, is found by solving Eq. (5) with surface Hamiltonian $H_S=H_L+H_R$, and where G is expanded in a double basis of RLAPWs. From the Green's function we obtain the local density of states $n(\boldsymbol{r};w)=-\pi^{-1}$ Im Tr $G(\boldsymbol{r},\boldsymbol{r};w)$, charge density, and other electronic properties. Self-consistent calculations are performed within the local density approximation (LDA) to density-functional theory, using the Perdew-Zunger parametrization of the exchange-correlation potential.[32] We assume an ideal unrelaxed structure with lattice parameter 4.08 Å. Our basis sets contain interstitial plane waves up to 220 eV, spin-angular functions within atomic spheres (radii 1.395 Å) corresponding to $\ell_{\max}=9$.

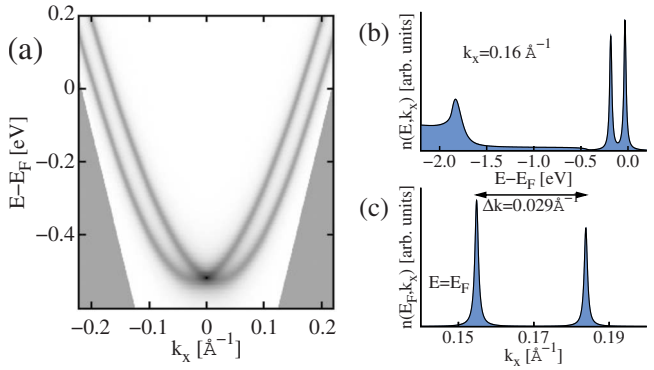

FIG. 9. (Color online) Results for the Au(111) surface state obtained using the relativistic embedding method including a single atomic layer within the embedded volume. (a) Intensity plot of the local density of states (LDOS) $n(E,k_x)$ for k_x along ΓK, calculated with Im $E=10^{-4}$ Ha. The shaded area is the bulk continuum. (b) LDOS for fixed $k_x=0.16$ Å^{-1}, showing the bulk continuum and spin-orbit split surface state. (c) LDOS at $E=E_F$ showing the wave-vector splitting of the surface state.

The valence density is found by integrating the Green's functions around a semicircular contour extending from extending from just below the valence band up to the Fermi level, evaluated using 31 Gauss-Chebyshev points, and using the equivalent of 486 k points in the full two-dimensional Brillouin zone.[33]

In Fig. 9(a) we illustrate results obtained for the dispersion of the zone-center surface state found in a calculation in which just the outermost layer of atoms is included in the embedded region. The dispersion is obtained from calculations of the energy and wave-vector-resolved local density of states, integrated over the surface region, and which is evaluated with a small imaginary component in the energy to broadens spectral features and aid their identification. The surface state clearly exhibits the characteristic spin-orbit splitting and is easily distinguished from bulk states and resonances even in this one layer calculation as the embedding potential ensures that the bulk continuum is faithfully reproduced, Fig. 9(b). Calculating the expectation value of the spin operator in the surface state we find, in agreement with both experiment[29,34,35] and previous theoretical calculations,[29,31,35] that the electron spin vectors lie in the surface plane and perpendicular to the electron momentum.

In Table I we compare the dispersion parameters and the wave-vector splitting at the Fermi energy found in our calculations [Fig. 9(c)] with those obtained in previous calculations and those observed in angle-resolved photoemission experiments on Au(111) surfaces and a vicinal surface with (111) terraces. The wave-vector splitting that we find agrees well with previous calculated values and those from experi-

TABLE I. Compilation of theoretically determined Au(111) surface state dispersion parameters and results from angle-resolved photoelectron spectroscopy experiments. Some key calculation details are noted. LDA and generalized gradient approximation (GGA) refer to different treatments of exchange-correlation effects in the density-functional theory. FLAPW indicates the full-potential calculations using two-component linearized augmented plane waves with variational inclusion of spin-orbit interaction. Further details may be found in the cited articles.

E_0 (eV)	m^*/m_e	k_f (Å^{-1})	Δk_f (Å^{-1})	Notes
			Theory	
−0.39			0.025	23 layer slab, LDA, FLAPW, Ref. 36
−0.50	0.23		0.023	Semi-infinite crystal, LDA+image barrier, atomic sphere, Ref. 31
−0.51	0.20	±0.149, 0.172	0.023	Semi-infinite crystal, LDA, muffin-tin, Refs. 29 and 35
−0.484	0.22		0.031	23 layer slab, LDA, FLAPW, Ref. 3
−0.326	0.25		0.031	23 layer slab, GGA, FLAPW, Ref. 3
−0.52	0.24	±0.159, 0.191	0.032	24 layer slab, LDA, pseudopotential, Ref. 37
			0.028	23 layer slab, FLAPW, Ref. 38
−0.52	0.25	±0.155, 0.184	0.029	1 embedded layer, LDA, RLAPW, this work
−0.52	0.25	±0.155, 0.184	0.029	3 embedded layer, LDA, RLAPW, this work
			Experiment	
−0.417	0.25	±0.153, 0.176	0.023	Ref. 28
−0.487	0.255	±0.172, 0.197	0.025	Ref. 36
−0.487	0.255	±0.167, 0.192	0.025	Ref. 39
−0.439	0.254	±0.157, 0.184	0.026	Au(23,23,21), Ref. 40
−0.47	0.25	±0.160, 0.186	0.026	Ref. 35
−0.46	0.25		0.026	Ref. 34
−0.479	0.26	±0.172, 0.197	0.024	Ref. 3

ment, which are on average ~10% lower than theory. Significantly, an embedding calculation in which just the outermost surface layer is explicitly included in the embedded volume yields the same surface state dispersion and spin-orbit splitting as a calculation in which the three outermost layers are included. Since over 40% of the splitting originates from relativistic interactions deeper that the surface layer,[30] this demonstrates that the relativistic embedding potential correctly replicates the influence of the extended substrate on states within the embedded region.

VI. SUMMARY

Inglesfield's embedding method is a powerful tool for electronic-structure studies in extended systems which may be naturally divided into two or more distinct regions. In the present work we have presented extensions to the embedding method that enable practical calculations to be performed for surface and interface systems when relativistic effects are expected to be important. First, the concept of the transfer matrix used in the nonrelativistic theory has been adapted to match boundary values of solutions to the Dirac equation across an embedded region. In contrast to the second order nature of the Schrödinger equation, which means that the conventional transfer matrix is defined in terms of an amplitude and normal derivative on the surface, the Dirac equation is first order and no normal derivative boundary condition need be specified. Consequently the new transfer matrix involves only the amplitude of the four component wave function on the surface. We have shown that as in the nonrelativistic case the transfer matrix may be written in terms of Green's functions for the embedded region; by choosing these to satisfy zero-amplitude small-component boundary conditions a relatively simple form for the transfer matrix is obtained that formally resembles the nonrelativistic version but which generally differs in the $c \to \infty$ limit.

Application of the transfer matrix to the problem of finding the complex band structure including relativistic effects has been described and demonstrated; also the use of the eigenvectors of the transfer matrix in constructing an embedding potential that can replace semi-infinite substrates in subsequent embedding calculations. The embedding potential, a 2×2 matrix function in the relativistic formulation, is also shown to play an important role in formulating the transport problem across an embedded region. It enables the identification of channel functions that form an orthogonal set over the embedding surface and which form a natural representation for determining transmission across interfaces. We have used these channel functions to derive an expression for transmission across an interface in terms of the Green's function for the embedded region and the embedding potentials in the leads. In deriving this, the more subtle nature of the Dirac theory becomes apparent as time reversal of states is not achieved by simple complex conjugation.

In the final section we have illustrated a relativistic surface electronic-structure calculation within the full-potential implementation of the embedding method. We have chosen the well-studied Au(111) surface and presented the results of calculations in which just the outermost or outer three layers of atoms at Au(111) are explicitly included with the semi-infinite substrate replaced by an embedding potential that has been obtained from the Dirac transfer matrix and with the semi-infinite vacuum replaced by an analytic embedding potential. The surface state dispersion and spin-orbit splitting that we obtain agree with those found in previous calculations and photoelectron spectroscopy measurements. Both our one- and three-layer calculations give similar results, illustrating the ability of the relativistic embedding potential to correctly replicate the influence of an extended substrate, including relativistic effects, on electronic states within the embedded region.

ACKNOWLEDGMENTS

The authors wish to thank H. Ishida (Nihon University) for making available his computer codes implementing the conventional FLAPW embedding method and which have formed the basis of the relativistic implementation reported here. M.J. acknowledges the support of the UK EPSRC.

*s.crampin@bath.ac.uk

[1] J. E. Inglesfield, J. Phys. C **14**, 3795 (1981).
[2] J. E. Inglesfield, Comput. Phys. Commun. **137**, 89 (2001).
[3] F. Forster, A. Bendounan, F. Reinert, V. G. Grigoryan, and M. Springborg, Surf. Sci. **601**, 5595 (2007).
[4] J. B. A. N. van Hoof, S. Crampin, and J. E. Inglesfield, J. Phys.: Condens. Matter **4**, 8477 (1992).
[5] H. Ishida, Phys. Rev. B **57**, 4140 (1998).
[6] D. Wortmann, H. Ishida, and S. Blügel, Phys. Rev. B **66**, 075113 (2002).
[7] T. Ohwaki, H. Ishida, and A. Liebsch, Phys. Rev. B **68**, 155422 (2003).
[8] O. R. Davies and J. E. Inglesfield, Phys. Rev. B **69**, 195110 (2004).
[9] J. E. Inglesfield, S. Crampin, and H. Ishida, Phys. Rev. B **71**, 155120 (2005).
[10] T. Ohwaki, D. Wortmann, H. Ishida, S. Blügel, and K. Terakura, Phys. Rev. B **73**, 235424 (2006).
[11] H. Ishida and A. Liebsch, Phys. Rev. B **79**, 045130 (2009).
[12] J. E. Inglesfield and G. A. Benesh, Phys. Rev. B **37**, 6682 (1988).
[13] H. Ishida, Phys. Rev. B **63**, 165409 (2001).
[14] H. Ishida, Phys. Rev. B **75**, 205419 (2007).
[15] S. Crampin, J. Phys.: Condens. Matter **16**, 8875 (2004).
[16] D. Wortmann, H. Ishida, and S. Blügel, Phys. Rev. B **65**, 165103 (2002).
[17] S. Crampin, M. Nekovee, and J. E. Inglesfield, Phys. Rev. B **51**, 7318 (1995).
[18] M. I. Trioni, G. P. Brivio, S. Crampin, and J. E. Inglesfield, Phys. Rev. B **53**, 8052 (1996).

[19] H. Ishida, Surf. Sci. **388**, 71 (1997).
[20] T. Takeda, J. Phys. F: Met. Phys. **9**, 815 (1979).
[21] R. E. Stanton and S. Havriliak, J. Chem. Phys. **81**, 1910 (1984).
[22] S. G. Davison and M. Steslicka, *Basic Theory of Surface States* (Oxford University Press, Oxford, 1996).
[23] P. Mavropoulos, N. Papanikolaou, and P. H. Dederichs, Phys. Rev. Lett. **85**, 1088 (2000).
[24] S. Crampin, J. B. A. N. van Hoof, M. Nekovee, and J. E. Inglesfield, J. Phys.: Condens. Matter **4**, 1475 (1992).
[25] V. Heine, Proc. Phys. Soc. London **81**, 300 (1963).
[26] A. Dal Corso, A. Smogunov, and E. Tosatti, Phys. Rev. B **74**, 045429 (2006).
[27] A. Messiah, *Quantum Mechanics* (North-Holland, Amsterdam, 1962), Vol. II.
[28] S. LaShell, B. A. McDougall, and E. Jensen, Phys. Rev. Lett. **77**, 3419 (1996).
[29] J. Henk, A. Ernst, and P. Bruno, Phys. Rev. B **68**, 165416 (2003).
[30] G. Bihlmayer, Y. M. Koroteev, P. M. Echenique, E. V. Chulkov, and S. Blügel, Surf. Sci. **600**, 3888 (2006).
[31] J. R. McLaughlan, E. M. Llewellyn-Samuel, and S. Crampin, J. Phys.: Condens. Matter **16**, 6841 (2004).
[32] J. P. Perdew and A. Zunger, Phys. Rev. B **23**, 5048 (1981).
[33] S. L. Cunningham, Phys. Rev. B **10**, 4988 (1974).
[34] M. Hoesch, M. Muntwiler, V. N. Petrov, M. Hengsberger, L. Patthey, M. Shi, M. Falub, T. Greber, and J. Osterwalder, Phys. Rev. B **69**, 241401(R) (2004).
[35] J. Henk, M. Hoesch, J. Osterwalder, A. Ernst, and P. Bruno, J. Phys.: Condens. Matter **16**, 7581 (2004).
[36] G. Nicolay, F. Reinert, S. Hüfner, and P. Blaha, Phys. Rev. B **65**, 033407 (2001).
[37] R. Mazzarello, A. D. Corso, and E. Tosatti, Surf. Sci. **602**, 893 (2008).
[38] M. Nagano, A. Kodama, T. Shishidou, and T. Oguchi, J. Phys.: Condens. Matter **21**, 064239 (2009).
[39] F. Reinert, G. Nicolay, S. Schmidt, D. Ehm, and S. Hüfner, Phys. Rev. B **63**, 115415 (2001).
[40] A. Mugarza, A. Mascaraque, V. Repain, S. Rousset, K. N. Altmann, F. J. Himpsel, Y. M. Koroteev, E. V. Chulkov, F. J. Garcia de Abajo, and J. E. Ortega, Phys. Rev. B **66**, 245419 (2002).